Target Selection in Multistatic Microwave Breast Imaging Setup using Dielectric Lens

Daniela M. Godinho*, João M. Felício†‡, Carlos A. Fernandes‡, Raquel C. Conceição*
*Instituto de Biofísica e Engenharia Biomédica, Faculdade de Ciências da Universidade de Lisboa, 1749-016 Lisbon, Portugal, dgodinho94@gmail.com
†Centro de Investigação Naval (CINAV), Escola Naval, Almada, Portugal
‡Instituto de Telecomunicações, Instituto Superior Técnico, Universidade de Lisboa, Lisbon, Portugal

***Abstract*—Microwave Imaging (MWI) has been studied to aid early breast cancer detection. Current prototypes in more advanced stages of development include both monostatic or multistatic setups. However, multistatic configurations usually include a high number of antennas which consequently require complex and computationally-intensive signal processing algorithms to ensure a good target detection. We previously presented a novel approach using a dielectric lens which reduces the signal processing burden of multistatic setups, while ensuring good spatial resolution. In this paper, we evaluate this novel setup using an anatomically realistic breast phantom and its capability of selecting targets inside the breast. We show a successful detection of the targets using an artefact removal algorithm based on singular value decomposition when the Bessel beam is centered at the target location.**

***Index Terms*—bessel beam, breast cancer detection, dielectric lens, microwave imaging, multistatic setup, singular value decomposition.**

I. Introduction

Every year, more than 2 million new breast cancer cases are reported worldwide and this type of cancer is now the most common cancer among men and women [1]. Microwave Imaging (MWI) has shown potential to aid breast cancer detection and diagnosis [2], [3]. It has several advantages compared to currently used imaging modalities: it uses non-ionising radiation, it does not require breast compression and it is relatively low-cost [4].

Several radar MWI systems have been proposed in the last decades, either using monostatic (i.e. signals transmitted and received by the same antenna), or multistatic setups (i.e. signals transmitted by one antenna and received by the remaining ones). While monostatic systems may imply long acquisition times, the acquisition in multistatic systems may be faster. The latter type of systems may be susceptible to coupling effects between antennas which may hinder the target detection and therefore require more complex and computationally-intensive algorithms to allow a successful detection.

In a previous study [5], we presented a feasibility study of a novel approach using a dielectric Bessel lens which illuminates the breast with a pencil beam, decreasing the coupling effects between the antennas. Promising results were obtained with a spherical breast phantom and an ideal calibration (i.e. subtracting simulated signals with and without targets). In this paper, we further evaluate this setup using a homogeneous anatomically realistic breast phantom and consider a realistic calibration where the target position is not known. We apply an automated artefact removal algorithm and compare the obtained 3D imaging results with an equivalent setup using just the lens primary feed as the active antenna, without the dielectric lens.

II. Simulated setups

The proposed setup is designed assuming the patient is lying in the prone position, with the breast extending through an opening on an examination table. It is a dry imaging system, which means both the breast and the antennas are placed in air. The dielectric lens and the respective primary feed are placed below the breast, and a second single antenna scans around the breast in a circular configuration in a total of 12 positions. We use a planar slot-based single-layer printed antenna formed by two crossed exponential slots (in short, XETS), impedance-matched from 2 to 6 GHz. The XETS type antenna is used both for the stand-alone receiving antenna scanning around the breast, and for the primary feed of the dielectric lens. The assembly of XETS and the Bessel lens works as the transmitting antenna. Both the setup and the antenna are described in more detail in [5]. All these elements were designed and simulated using the Computer Simulation Technology (CST) Studio software [6].

A realistic breast phantom [7] is considered for the hereby presented tests. The phantom is homogeneous with relative permittivity $\epsilon_r = 8$ and dissipation factor $\tan(\delta) = 0.1$, which approximately corresponds to the upper limit of fat permittivity [8]. Two spherical Perfect Electric Conductor (PEC) targets with a 5 mm radius are placed inside the realistic breast. They are placed asymmetrically, at coordinates $(x, y) = (30, 0)$ and $(x, y) = (-30, 10)$ mm and at the same z plane (50 mm from the nipple surface. These targets will be called T1 and T2 from now on, respectively.

The results with the same setup with and without the lens (Fig. 1) are compared. The distance between the XETS behind the lens and the surface of the sphere is 255 mm, while between the stand-alone XETS (when it is used without the lens) and the surface is 115 mm. This ensures the same incident field level on the breast in both configurations. In both cases, the XETS below the breast is placed in three positions $x = [-30;\ 0;\ 30]$ mm, in order to evaluate if this setup allows selecting only one target

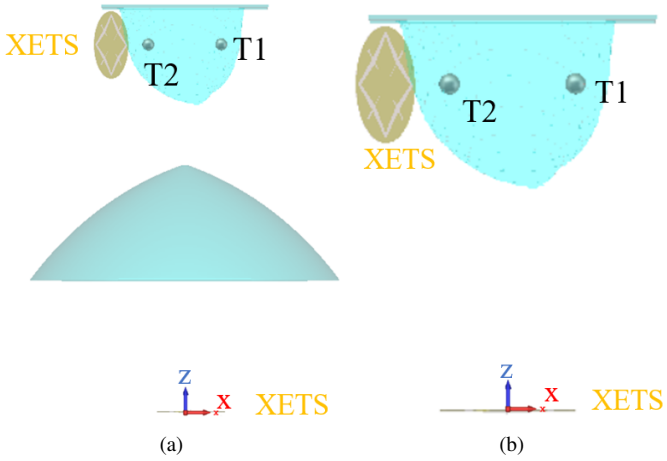

(a) (b)

Fig. 1. Multistatic setup with a homogeneous breast phantom with two PEC targets and one example of the position of the XETS around the breast and (a) the XETS and Bessel lens at the bottom and (b) the XETS as a stand-alone antenna at the bottom.

and evaluate as well other differences between XETS and the assembly XETS+Lens. The Bessel lens is not shifted. Shifting the XETS as a stand-alone antenna to one position yields a similar result if the XETS below the lens is shifted to the opposite direction, as shown in Figure 2.

III. Signal Processing

This section presents the signal processing algorithms used to process the microwave signals: artefact removal and image reconstruction algorithms.

A. Artefact Removal Algorithm

The skin response artefact is one of the main artefacts in MWI. Our breast phantom does not include a skin layer but in a dry imaging setup there is an air-phantom interface with a dielectric contrast which also creates a high magnitude response in an early-time response.

We use Singular Value Decomposition (SVD) as artefact removal algorithm, which has been used for monostatic air-operated imaging setups [9], [10]. SVD computes the factorisation of a real or complex matrix $\mathbf{M}$ of signals into three matrices of singular vectors and singular values [9]. The first singular vectors contain high magnitude responses which are likely caused by the air-phantom interface response. The signals without that response can be obtained by subtracting the contribution of a number n_{sv} of singular vectors to each signal. An automated procedure is needed in order to find the optimal n_{sv} which successfully removes the artefacts and maintain the target response.

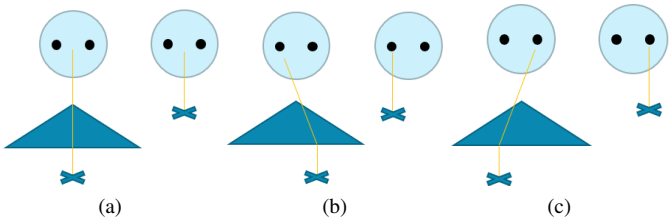

(a) (b) (c)

Fig. 2. Illustration of the XETS positions for the setup with and without the lens in (a) a centred position, (b) focusing T1, and (c) focusing T2. The light blue circle represents the breast phantom, the black circles represent the targets, the dark blue triangle represents the lens, the blue cross represents the antenna, and the yellow line represents the direction of the beam.

In this work, the algorithm is adapted for a multistatic imaging setup. Each column of $\mathbf{M}$ corresponds to the input transmission coefficient $\mathbf{s}_{i,j}$, where i corresponds to the XETS below the breast (the transmitting antenna) and j corresponds to each position of the XETS that rotates around the breast (the receiving antenna positions), and each row corresponds to each frequency point of $\mathbf{s}_{i,j}$. The $\mathbf{s}_{i,j}$ is obtained from the difference between the simulated response from all components and the simulated response of the same setup without the breast and targets, to remove the antenna response.

To remove the artefact response from each input signal, matrix $\mathbf{M}$ is created considering the three neighbouring antennas for each side of the main antenna position $\mathbf{s}_{i,j-3}$, $\mathbf{s}_{i,j-2}$, $\mathbf{s}_{i,j-1}$, $\mathbf{s}_{i,j}$, $\mathbf{s}_{i,j+1}$, $\mathbf{s}_{i,j+2}$, $\mathbf{s}_{i,j+3}$. The distances between each pair of antennas and the air-breast interface need to be calculated. Fig. 3 shows how the distances are calculated between each pair of antennas. The minimum ($\min_d$) and the maximum ($\max_d$) distances are calculated considering the distance between antenna j to the closest and farthest entry point in the phantom, respectively, and the distance between that entry point to antenna i. Then, the optimal number of singular vectors to remove (n_{sv}) is found by applying an automatic procedure that ensures the response of the air-phantom interface is minimised. The six resulting multistatic signals after removing 1 to 6 singular vectors from the original input signal are analysed, considering the ratios between the magnitudes of each signal at the minimum ($m_{\min_d}$) and maximum ($m_{\max_d}$) distances to the air-phantom interface and the maximum magnitude of each signal (m_{sv}). The optimal number n_{sv} corresponds to the first resulting signal where the following criteria are met: $m_{\min_d}/m_{sv} \leq 0.5$ and $m_{\min_d}/m_{sv} + m_{\max_d}/m_{sv} \leq 1$.

B. Image Reconstruction Algorithm

The reconstructed images are created in three dimensions and using an image reconstruction algorithm based on the wave migration algorithm. The intensity of each voxel is calculated considering the input transmission signals $\mathbf{s}_{i,j}$ after artefact removal and calculated distances between each antenna position and each voxel, as explained in [5].

The quality of the reconstructed images are evaluated using state-of-the-art performance metrics: Signal-to-Clutter Ratio (SCR), Signal-to-Mean Ratio (SMR), Full Width Half Maximum (FWHM) and Localisation Error (LE) [10].

IV. Results and Discussion

In this section we present the main imaging results of our study and the corresponding quantitative evaluation. Fig. 4 shows an example of the multistatic signals between one pair of antenna positions of the setup with the lens, when removing 1

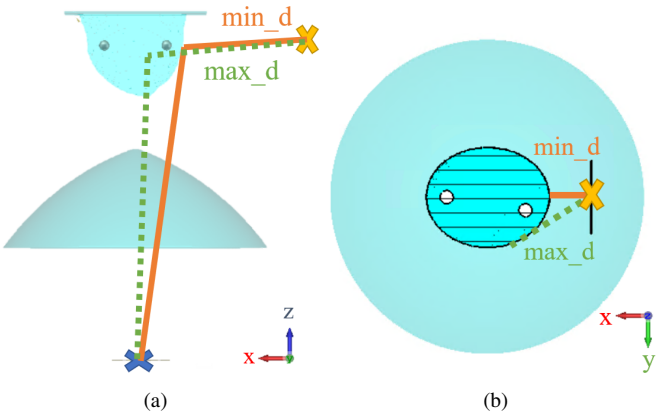

(a) (b)

Fig. 3. Illustration of calculation of minimum and maximum distances to the air-phantom interface for one pair of antennas in (a) xz and (b) xy planes. The orange and green lines represent the minimum and the maximum distances between the two antenna positions to the air-phantom interface, respectively.

to 6 singular vectors resulting from SVD. The plots indicate there is still an early-time high magnitude response when 1 or 2 singular vectors are removed. The highest response of the remaining signal matches the location of the target when 3 singular vectors are removed. Indeed, in this case, our automated criteria chose $n_{sv} = 3$, by minimising the magnitude at the calculated distances to the air-phantom interface.

Table I summarises the performance metrics of each 3D reconstructed image. It includes the results of the setups with and without the lens and the three positions of the XETS below the breast. The region of T1 is illuminated when the stand-alone XETS is placed at $x = 30$ mm and the XETS below the lens is placed at $x = -30$ mm. The region of T2 is not completely illuminated in neither of these cases since no shift of the XETS in the y-axis was simulated but the case with more illumination in the T2 region happens when the stand-alone XETS is placed at $x = -30$ mm and the XETS below the lens is placed at $x = 30$ mm.

TABLE I
PERFORMANCE METRICS OF THE RECONSTRUCTED IMAGES.

	Focus region					
	XETS			***XETS + Lens***		
Metrics	***-30***	***0***	***30***	***-30***	***0***	***30***
SCR (dB)	0.5	0.2	1.3	1.9	1.4	0.8
SMR (dB)	8.9	8.5	9.3	11.2	9.7	8.9
FWHM T1 (mm)	6.3	9.0	7.7	14.3	13.3	18.0
FWHM T2 (mm)	2.3	14.0	13.7	4.7	7.3	16.3
LE T1 (mm)	47.9	35.9	57.8	**7.0**	35.4	41.2
LE T2 (mm)	53.0	43.2	31.0	61.2	43.9	**15.9**

The results show SVD is not able to successfully remove the artefacts when the XETS is placed at $x = 0$ mm in both type of setups: with and without the lens. However, targets are better detected when the Bessel lens is present in the setup. When the XETS is shifted to $x = -30$ mm, T1 is illuminated and

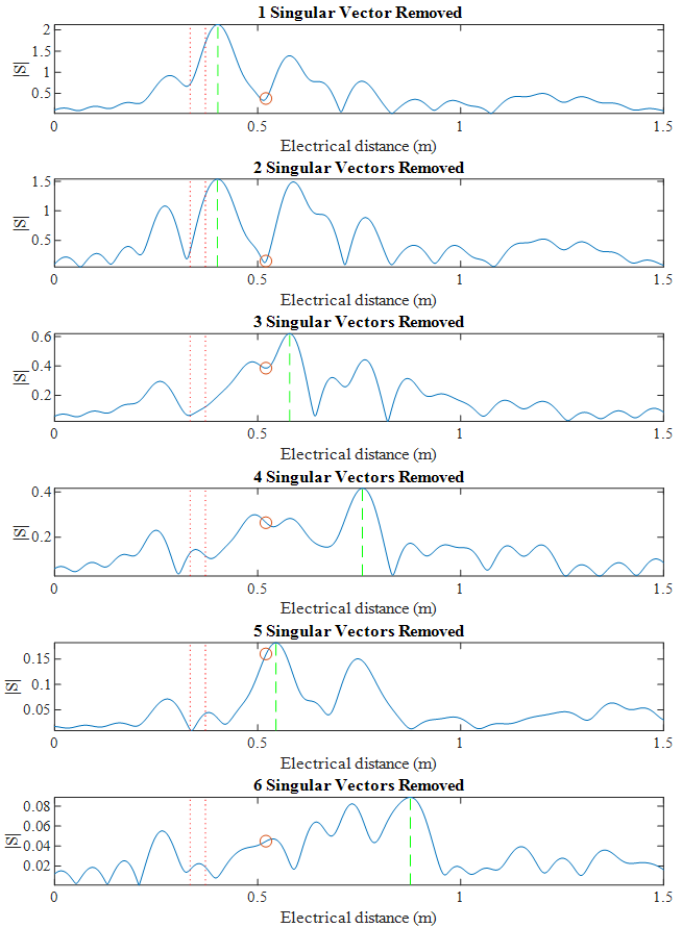

Fig. 4. Multistatic signals between the antenna position 4 and the antenna below the breast when removing 1 to 6 singular vectors over electrical distance. The first and second red vertical lines correspond to minimum ($\min_d$) and maximum ($\max_d$) distances between the pair of antennas and the air-phantom interface, respectively. The green vertical line correspond to the maximum of the signal and the red circle correspond to the electrical distance between the pair of antennas and the target. The input coefficients $\mathbf{s}_{i,j}$ have no units.

detected with a LE of 7 mm on the z-axis. The SCR and SMR are also reasonable for a positive detection, as also observed in Fig. 5. When the XETS is shifted to $x = 30$ mm, T2 is detected, with a LE of 15.9 mm (observed mainly in the z-axis), but with some artefacts, as shown in Figure 6. As mentioned before, the weakened detection of T2 may be explained by the fact that the region of T2 is intentionally not properly illuminated by the Bessel beam.

The air-phantom interface artefacts are more difficult to remove from the multistatic signals when the stand-alone XETS is used below the breast. As shown in Fig. 7, when the XETS is placed at $x = -30$ mm, only the T1 is detected but there are some artefacts near the air-phantom interface. The highest intensity voxel of the 3D volume is not located in the 2D planes shown in the figure, which explains the high LE. Because this position was not directly illuminating the region of T1, we did not expect to detect this target using this position. However, the positive detection of T1 and the negative detection of T2

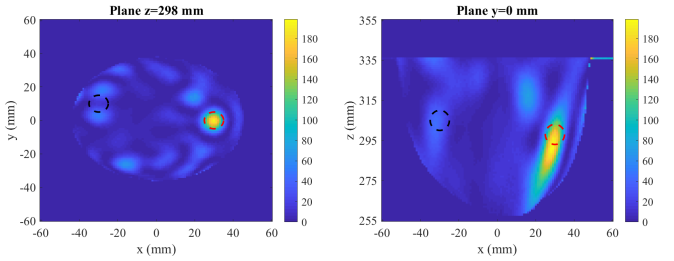

(a) (b)

Fig. 5. Reconstructed images of realistic breast phantom with two PEC targets inside using XETS and the Bessel lens, where XETS is placed at $x = -30$ mm. The images are represented in (a) xy and (b) xz planes and correspond to the planes of the highest voxel in the 3D volume. The real size and location of the targets are represented by dashed circles, the red circle corresponds to T1 and the black circle corresponds to T2. The image intensities have no units.

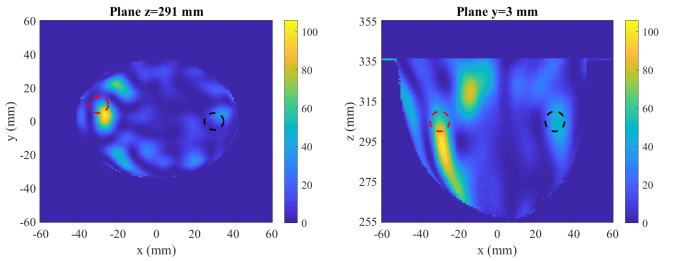

(a) (b)

Fig. 6. Reconstructed images of realistic breast phantom with two PEC targets inside using XETS and the Bessel lens, where XETS is placed at $x = 30$ mm. The images are represented in (a) xy and (b) xz planes and correspond to the planes of the highest voxel in the 3D volume. The real size and location of the targets are represented by dashed circles, the red circle corresponds to T2 and the black circle corresponds to T1. The image intensities have no units.

may be a result of the higher coupling between the receiving antenna positions closest to T2 and the transmitting antenna and lower coupling between the receiving antennas closest to T1 and the transmitting antenna. The receiving antennas closest to T1 can still record the response of the target due to the large beam of the XETS, in contrast to the Bessel beam, which allows sufficient transmission between the pair of antennas. Nonetheless, in all three cases with the stand-alone XETS, the LE is higher than 30 mm, mainly due to small artefacts near the air-phantom interface which mask the targets response.

V. Conclusion

Our results showed the Bessel lens has the ability to illuminate certain regions of the breast and improve the artefact removal performance, by decreasing the coupling effects between antennas that may require complex signal processing algorithms. This setup outperforms an equivalent setup without the lens, where the artefacts are more challenging to remove.

In future work, experimental validation is still needed, as well as considering larger and more complex phantoms, with different Breast Imaging-Reporting and Data System (BI-RADS) categories, which are computationally heavy to simulate. These

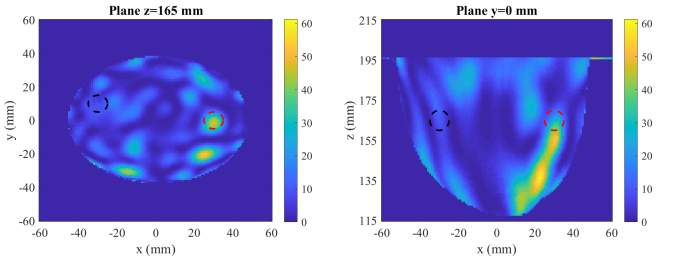

(a) (b)

Fig. 7. Reconstructed images of realistic breast phantom with two PEC targets inside using stand-alone XETS, where XETS is placed at $x = -30$ mm. The images are represented in (a) xy and (b) xz planes and correspond to the planes of the targets. The real size and location of the targets are represented by dashed circles, the red circle corresponds to T1 and the black circle corresponds to T2. The image intensities have no units.

types of breasts can also provide more evidence to the advantages of using the Bessel lens.

Acknowledgment

This work is supported by Fundação para a Ciência e a Tecnologia-FCT under the fellowship SFRH/BD/129230/2017, FCT/MEC (PIDDAC) under the Strategic Programme UIDB/00645/2020, and also in part by FEDER-PT2020 Partnership Agreement under Grant UIDB/EEA/50008/2020. This work is developed in the framework of COST Action CA17115 – MyWAVE.

References

[1] The Global Cancer Observatory - World Health Organization, "GLOBOCAN 2020: Estimated Cancer Incidence, Mortality and Prevalence Worldwide in 2020," 2020. [Online]. Available: http://gco.iarc.fr/today

[2] A. Fasoula, L. Duchesne, J. D. G. Cano, P. Lawrence, G. Robin, and J.-G. Bernard, "On-Site Validation of a Microwave Breast Imaging System, before First Patient Study," *Diagnostics*, vol. 8, no. 53, pp. 1–38, 2018.

[3] M. Klemm *et al.*, "Clinical Trials of a UWB Imaging Radar for Breast Cancer," in *4th European Conference on Antennas and Propagation (EuCAP)*, Barcelona, Spain, 2010.

[4] R. C. Conceição *et al.*, *An Introduction to Microwave Imaging for Breast Cancer Detection*, ser. Biological and Medical Physics, Biomedical Engineering, R. C. Conceição, J. J. Mohr, and M. O'Halloran, Eds. Switzerland: Springer, 2016.

[5] D. M. Godinho, J. M. Felício, C. A. Fernandes, and R. C. Conceição, "Feasibility study of focal lens for multistatic microwave breast imaging," in *23rd International Conference on Applied Electromagnetics and Communications (ICECOM)*, Dubrovnik, Croatia, 2019.

[6] Dassault Systèmes, "CST – Computer Simulation Technology," 2021. [Online]. Available: https://www.3ds.com/products-services/simulia/products/cst-studio-suite/

[7] M. J. Burfeindt *et al.*, "MRI-Derived 3-D-Printed Breast Phantom for Microwave Breast Imaging Validation," *IEEE Antennas and Wireless Propagation Letters*, vol. 11, pp. 1610–1613, 2012.

[8] M. Lazebnik *et al.*, "A large-scale study of the ultrawideband microwave dielectric properties of normal breast tissue obtained from reduction surgeries," *Physics in Medicine and Biology*, vol. 52, no. 10, pp. 2637–3656, 2007.

[9] J. M. Felício, J. M. Bioucas-Dias, J. R. Costa, and C. A. Fernandes, "Microwave Breast Imaging using a Dry Setup," *IEEE Transactions on Computational Imaging*, vol. 6, pp. 167–180, 2020.

[10] D. M. Godinho, J. M. Felício, C. A. Fernandes, and R. C. Conceição, "Experimental Evaluation of an Axillary Microwave Imaging System to Aid Breast Cancer Staging," *IEEE Journal of Electromagnetics, RF, and Microwaves in Medicine and Biology*, 2021. doi:10.1109/JERM.2021.3097877.